



Contents lists available at ScienceDirect

Journal of Colloid and Interface Science

journal homepage: www.elsevier.com/locate/jcis

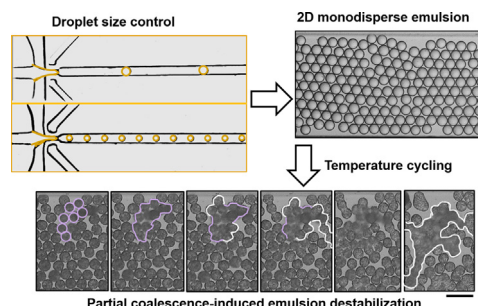
Regular Article

Microfluidic production of size-tunable hexadecane-in-water emulsions: Effect of droplet size on destabilization of two-dimensional emulsions due to partial coalescence

Samira Abedi, Naureen S. Suteria, Chau-Chyun Chen^{*}, Siva A. Vanapalli^{*}

Department of Chemical Engineering, Texas Tech University, Lubbock, TX 79409-3121, USA

GRAPHICAL ABSTRACT



ARTICLE INFO

Article history:

Received 24 May 2018

Revised 15 August 2018

Accepted 16 August 2018

Available online 17 August 2018

Keywords:

Microfluidics

Valve-based flow-focusing device

Monodisperse oil-in-water emulsions

Partial coalescence

Multi-body coalescence

ABSTRACT

Hypothesis: Despite numerous studies, the mechanism of destabilization of oil-in-water emulsions during cooling-heating cycles is unclear due to indirect measurements and lack of direct control over the droplet size. It is hypothesized that emulsions with a smaller droplet size are more resistant to destabilization than emulsions containing larger droplets since the probability of initiating partial coalescence and forming large-scale aggregates is lower for small droplets.

Experiments: Monodisperse hexadecane-in-water emulsions with controlled droplet sizes were produced using a microfluidic valve-based flow-focusing device and varying the system parameters. A unique approach was developed to create a two-dimensional (2D) array of droplets enabling visualization of the destabilization process due to temperature cycling. The influence of droplet size on partial coalescence and destabilization was investigated.

Findings: In the 2D emulsion, destabilization proceeds through a combination of spontaneous coalescence events that yield small-scale structures followed by formation of large-scale structures by coalescence propagation. We find that emulsion destabilization increases with droplet size. Quantifying the frequency of n -body coalescence events reveals that in emulsions with small droplets coalescence propagation is hindered. Phenomena involving restructuring, growth and cross-linking of droplet aggregates are identified as the key features of the emulsion destabilization mechanism.

© 2018 Published by Elsevier Inc.

1. Introduction

Oil-in-water emulsions form the basis of numerous manufactured products such as pharmaceuticals, foods, agro-chemicals,

^{*} Corresponding authors.

E-mail addresses: chauchyun.chen@ttu.edu (C.-C. Chen), siva.vanapalli@ttu.edu (S.A. Vanapalli).

paints, and cosmetics. Not only do they enhance the physical properties of the products, but they can also facilitate the encapsulation, preservation, and drug delivery of non-polar components such as vitamins, flavors, and antimicrobials [1–4]. Important properties, such as rheology and stability of these emulsion-based systems, strongly depend on the droplet size distribution, composition, volume fraction, interfacial properties, and physical state of the droplets [5,6]. In fact, tight control of the parameters, such as droplet size and volume fraction, in emulsions is necessary to prevent emulsion destabilization mechanisms such as flocculation, creaming, Ostwald ripening, and coalescence [7–11].

Commercial emulsion-based products often contain a mixture of lipids [12], which makes it difficult to understand the contribution of the individual lipids to the physicochemical properties of the emulsions. To address this, model emulsions with well-defined size and composition have been widely used [13,14]. In this regard, *n*-alkanes have been great candidates to produce model oil-in-water emulsions. Although the chemical structure of *n*-alkanes is simple, they form the basis of many derivative molecules, thus making them a useful model system [15]. Among *n*-alkanes, hexadecane, with a melting point of 18 °C [16], is a liquid at room temperature and is easy to handle for emulsification. Therefore, during the past decades, hexadecane-in-water (HiW) emulsions have been employed as a model system for emulsion studies. Some of the key phenomena studied in HiW emulsions include creaming [7], coalescence [17], Ostwald ripening [18], rheology [7], nucleation [16,19], assembly of droplet structures [20], and self-shaping [21].

Most studies employing hexadecane as the dispersed phase apply homogenization and fractionation techniques [22,23] to make the emulsions. Homogenization involves generating a polydisperse emulsion with a high-pressure valve homogenizer. Consequently, fractionation is induced by depletion flocculation to obtain relatively monodisperse emulsions. Depending on the amount of surfactant added, droplets larger than a critical size will flocculate, leaving the smaller droplets intact. By gravitational separation of the flocculated droplets and repeating this procedure several times, emulsions with different mean droplet sizes have been obtained [7]. Besides being tedious, these methods offer no direct control over the size of the individual droplets. The lowest polydispersity index (PDI) reported using such techniques has been 10–15% [16], which can preclude detailed understanding of the physicochemical phenomena in emulsions that are sensitive to droplet size [16,24].

To generate emulsions of controlled and narrow size distribution (PDI < 5%), microfluidics [25,26] has shown great promise. Various geometries, such as *T*-junction [17] and flow-focusing [27], have been designed for producing monodisperse microfluidic emulsions. In a *T*-junction device, the interaction of two immiscible fluids flowing perpendicular to each other leads to the formation of monodisperse droplets [26,28]. In this geometry, the droplet size can be controlled by adjusting the flow rate ratio of the two fluids [29–31]. However, changes in the flow rate may lead to slow response time and alter the device performance [32]. Flow-focusing devices (FFD) also offer an efficient way to produce monodisperse emulsions [33]. The droplet size in the FFD, when operated in the dripping regime [33], is proportional to the width of the drop formation orifice [34] and does not depend significantly on the flow rate ratio [33]. As a result, it is difficult to fine-tune the droplet size over a wide range in an FFD device without changing the orifice width. Nevertheless, studies have made HiW emulsions using these techniques [17,35].

Recently, to dynamically control the droplet size with a fast response time, Abate et al. implemented a membrane valve adjacent to the orifice in the FFD, which can be pressurized to deform the orifice walls and therefore change the orifice size [32]. They

tested this system by generating monodisperse *water-in-oil* emulsions and showed that the droplet size could be tuned from 7 to 200 μm . They found a nonlinear relation between the droplet size and orifice width which they attributed to the increase in the local velocity due to the reduction in the orifice width. To date, such a flexible and robust approach has not been applied to the generation of HiW emulsions. Since these emulsions are widely studied as a model system, it is essential to identify the operating conditions for generating monodisperse HiW emulsions in a valve-based flow-focusing device (V-FFD). Knowledge from such an investigation will enable widespread use of monodisperse HiW emulsions for fundamental studies in emulsion-science.

Monodisperse microfluidic emulsions could particularly provide valuable insights into the stability of emulsions. Emulsions could break down over time through different processes such as creaming, flocculation, coalescence and Ostwald ripening [7,18]. Phase transition could also affect the stability of the emulsions due to partial coalescence, where two or more partially crystalline droplets merge, forming non-spherical aggregates [36–39]. The non-spherical shape is maintained when the elastic stresses due to the crystalline network, dominate the interfacial stresses [40]. Studies have shown that partial coalescence-induced destabilization of emulsions during cooling-heating cycles depends on oil type, volume fraction, droplet size, surfactant type, aqueous phase composition, shear rate, and cooling rate [10,36–39,41–44]. These studies used polydisperse emulsions made through homogenization and studied emulsion destabilization using indirect methods such as differential scanning calorimetry and rheometry.

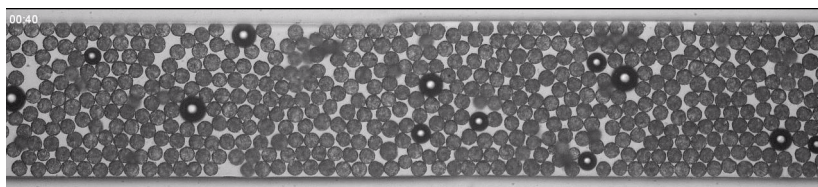
More recently, using micromanipulation techniques and direct observations, Spicer and co-workers studied the stability of partially coalesced doublet and triplet structures. For doublets, they showed that the stability depends on the competition between elastic and interfacial stresses, which can be controlled by the volume fraction of crystalline content in the droplets [40]. In case of triplets, they found that the droplets can restructure into a more compact packing arrangement without fully coalescing [45]. This restructuring was shown to occur due to the expansion of meniscus that connects the droplets, resulting in the minimization of the surface energy of the triplet. It remains to be ascertained how these important insights play out when studying larger populations of droplets that model real emulsions.

The goal of this work is two-fold. First, we use the V-FFD to identify the flow and valve-actuation conditions that produce monodisperse HiW emulsions of tunable size. Second, we employ the microfluidic HiW emulsions and use microscopy to visualize and directly measure the *in situ* destabilization of a two-dimensional (2D) array of droplets during a cooling-heating cycle. Subsequently, we demonstrate the impact of droplet size on destabilization of the 2D emulsion due to partial coalescence. To the best of our knowledge, visualization of partial coalescence using monodisperse emulsions have not been conducted to date, since it is difficult to achieve with traditional methods.

2. Materials and methods

2.1. Design and fabrication of microfluidic devices

For this study, two microfluidic devices were fabricated. One was a valve-based flow-focusing device (V-FFD) (Fig. 1a) for droplet generation, and the other was a long serpentine channel (Fig. 1b) to store the droplets. Based on the design of Abate et al. [32], the V-FFD had a flow-focusing junction with a membrane valve on both sides of the orifice, as shown in Fig. 1a. When air pressure was applied to the membrane valves, the width of the flow-focusing orifice decreased, thereby reducing the size of



Supplementary Video 1.

generated droplets (See [Supplementary Video 1](#)). The orifice width and height of the V-FFD were $39 \pm 1 \mu\text{m}$ and $58 \pm 2 \mu\text{m}$, respectively. The valve channels had a width of $22 \pm 1 \mu\text{m}$, and the wall thickness between the membrane valves and the flow focusing orifice was $17 \pm 1 \mu\text{m}$. A 30 cm long serpentine storage device with a width of $472 \pm 12 \mu\text{m}$ and a height of $98 \pm 2 \mu\text{m}$ was designed to store and immobilize the HiW emulsions.

Masters for the droplet generation and the storage devices were fabricated using a negative photoresist (SU-8 2050, MicroChem) with standard photolithographic methods [46]. The replicas of the V-FFD devices were cast in poly-dimethyl-siloxane (PDMS, Sylgard 184, Dow Corning) using soft-lithography [46]. To make the membrane valves flexible in response to air pressure, a 12:1 ratio of monomer to crosslinker was used [32], and the PDMS was cured at 65°C for two hours. After fluidic ports were made in the PDMS replicas with a 1 mm diameter biopsy puncher (Miltex), they were exposed to oxygen plasma for one minute (Harrick Plasma Cleaner) and immediately bonded to a glass slide.

Droplet storage devices were fabricated using Norland Optical Adhesive 81 (NOA81, Norland Products) [47]. First, NOA81 was

poured onto the SU-8 master and cured in three steps of 10 s, under UV radiation (Loctite 7411-S UV curing system). The NOA81 layer was removed from the SU-8 mold, and the fluidic and temperature measurement ports were made using a 1.5 mm biopsy punch (Miltex). The NOA81 chip was cleaned with isopropanol and air dried. Then, a glass slide was covered with a thin layer of NOA81 and was exposed to UV for 15 s. The coated glass slide and the NOA81 chip were bonded after 60 s oxygen plasma cleaning. The device was exposed to UV light for 20 s and heat-treated at 65°C for 15 min to ensure complete and permanent sealing. Tygon tubing (Cole Parmer) was glued to fluidic and temperature measurement ports (for insertion of thermocouples) with 5-minute epoxy (Devcon).

2.2. Droplet generation

The HiW emulsion droplets were generated using deionized water containing 2 wt% of sodium dodecyl sulfate (SDS, Sigma Aldrich) and hexadecane (Sigma Aldrich, purity > 99%) as the continuous and dispersed phases, respectively. All reagents were used

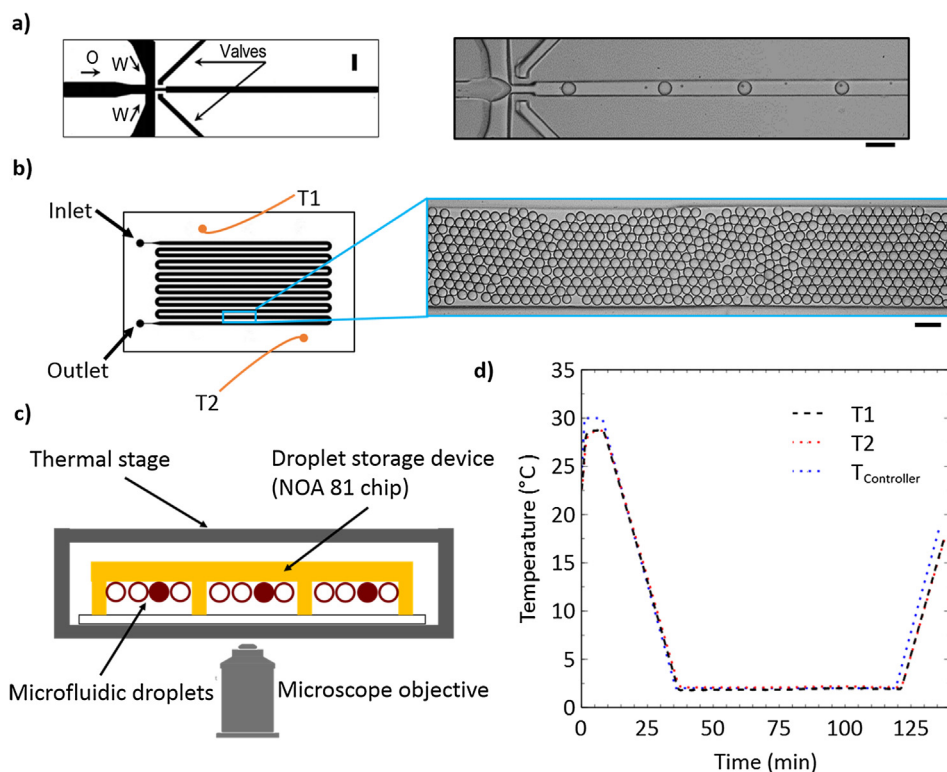


Fig. 1. Microfluidic production of monodisperse emulsions for studying partial coalescence. (a) Schematic of the valve-based flow-focusing device based on the design of Abate et al. [1] (left). Image showing the emulsion production (right) (See [Supplementary Video 1](#)). Black arrows indicate the valve channels that are controlled by air pressure. W and O indicate water and oil inlets respectively. (b) Schematic of droplet storage device. The long serpentine channel helps to immobilize the droplets in a single layer. The temperature is measured at two locations in the device, denoted by orange dots. The blue rectangle indicates the field of view in which the emulsions are monitored during the temperature cycling. Here, the mean droplet diameter is $40 \mu\text{m}$. (c) Schematic (side-view) of experimental setup for performing temperature cycling experiments. The NOA81 droplet storage device containing C16 emulsions is placed in a thermal stage. The light and dark droplets represent liquid and solid C16 droplets, respectively. (d) Plot of the temperature in device measured by the thermocouples (T1 and T2) and recorded by the temperature controller software ($T_{\text{Controller}}$) during the cooling-heating cycle. Scale bars in (a) and (b) denote $100 \mu\text{m}$. (For interpretation of the references to color in this figure legend, the reader is referred to the web version of this article.)

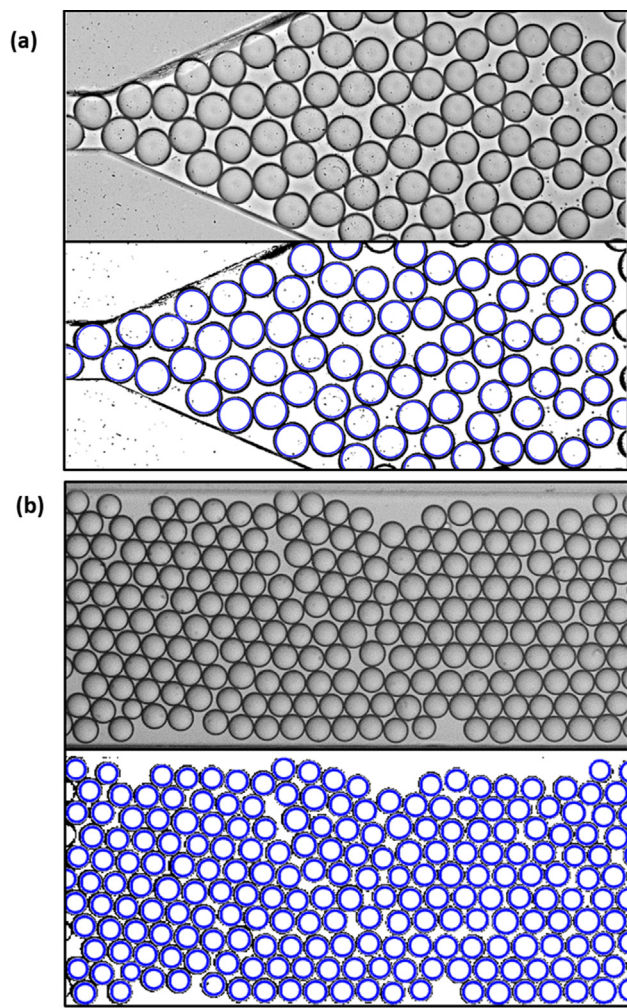


Fig. 2. Image processing for droplet detection and size measurements. (a) Experimental image of pancake droplets downstream of the V-FFD (top) and their corresponding processed image (bottom). The water and oil flow rate are each 50 $\mu\text{L/hr}$. (b) Experimental image of 40 μm droplets immobilized in the droplet storage device (top) and their corresponding processed image (bottom). In both a and b, the detected circles are visualized by a blue outline. Scale bar is 100 μm and is the same for all images. (For interpretation of the references to color in this figure legend, the reader is referred to the web version of this article.)

as received without further purification. The flow rates of the continuous and dispersed phases were controlled using 1 mL gas-tight syringes (Hamilton) and syringe pumps (PHD2000, Harvard Apparatus). The valve channels were filled with water using a hand-held syringe and then pressurized with air. For membrane-valve actuation, the pressure of the air (P_v) was regulated using an electronic pressure controller (Marsh Bellofram, Type 3000) with an accuracy of 0.1 psi. We record images of the droplet generation in the V-FFD using a 20x objective, at a resolution of 1 $\mu\text{m}/\text{pix}$, and a frame rate of 1000 fps with a Nikon Ti Microscope and a high-speed camera (Phantom v710). Images were recorded both at the droplet generation site (Fig. 1a) and downstream of the device (Fig. 2a). The emulsions were collected in a long, coiled piece of Tygon tubing (ID = 0.02", length = 0.5 m), connected to the outlet of the droplet generation device, and were subsequently used in the temperature cycling experiments to investigate emulsion destabilization.

2.3. Droplet storage and temperature cycling

A long serpentine channel was used for the storage and immobilization of 2D droplet arrays (Fig. 1b) [48]. The emulsion

collected in the Tygon tubing at room temperature was gently injected into the storage channel using a syringe filled with SDS solution. The droplet diameter did not change during storage and with a gentle injection of the emulsion into the storage device. Consequently, the Tygon tubing was detached from the storage device, which allowed the droplets to slow down and become immobilized. The storage device was then sealed by blocking the ports with metal pins, which reduced the motion of the emulsions during the experiments. We find that even though the droplets (of diameter 20–40 μm) did not entirely occupy the channel of depth (100 μm), as shown in the inset of Fig. 2b., they formed a single layer. Since hexadecane droplets are lighter than the continuous aqueous phase (density difference $\Delta\rho = 230 \text{ kg/m}^3$) they cream in the storage channel. The top wall of the channel confines this creamed emulsion and guides the droplets to form a 2D arrangement. Also, the dilution of the emulsion and flow of droplets during the injection from the Tygon tubing prevented the formation of multiple layers of emulsions and enabled the formation of a single layer of 2D emulsions in the storage serpentine channel.

The characteristics of the emulsions used in the cooling-heating cycles are listed in Table 1, where we also report their respective volume fraction, surface coverage in the storage channel and the flow conditions used to create the emulsion with the V-FFD. The approximate average diameters of these emulsions are noted as 20, 25, 32, and 40 μm throughout the text. Here, the volume fraction was determined by the ratio of the total volume of droplets in the field of view (blue rectangular box in Fig. 1b) to the corresponding volume of the storage channel. Likewise, the surface fraction was determined by the ratio of the circular area of all the droplet in the field of view to the corresponding area of the storage channel.

2.4. Emulsion temperature cycling experiments

The schematic of the experimental setup for emulsion cooling and heating experiments is shown in Fig. 1c. Briefly, the emulsion-loaded storage device was transferred to a Peltier based thermal stage (TSA12Gi, Instec) that mounts on the microscope [49]. The thermal stage has a 1.5 cm diameter circular window for optical access. A programmable controller (mk2000, Instec) and accompanying software (Wintemp, Instec) regulated the temperature of the device using a refrigerated water bath that acted as a heat sink [49]. To monitor the storage device temperature during the experiments, we placed two thin wire thermocouples (5SC-TT-K-40-36, Omega) in the temperature measurement ports located on the storage channel (orange lines in Fig. 1b). The temperature was recorded at 1-second intervals using a data acquisition board (TC08, Omega) and Omega Logging software 5.21.6.

The temperature protocol used for partial coalescence studies is shown in Fig. 1d. Initially, the thermal stage temperature was held at 23 $^{\circ}\text{C}$. Then, the temperature controller was set to increase the temperature from 23 $^{\circ}\text{C}$ to 30 $^{\circ}\text{C}$ at the rate of 5 $^{\circ}\text{C}/\text{min}$ and held for 10 min to melt any potential crystallites. The temperature was then reduced to 2 $^{\circ}\text{C}$ at the rate of 1 $^{\circ}\text{C}/\text{min}$ and held there (for typically 20–90 min, depending on the droplet size) until all the liquid droplets were crystallized. Subsequently, the temperature was increased from 2 $^{\circ}\text{C}$ to 30 $^{\circ}\text{C}$ at the rate of 1 $^{\circ}\text{C}/\text{min}$. During cooling-heating cycle, we acquired images of the droplet arrays at 24 fps at 10x magnification and resolution of 2 $\mu\text{m}/\text{pix}$.

The temperature was recorded at locations T_1 and T_2 for every experiment (Fig. 1b). In Fig. 1d, we show the temperatures recorded by the controller as well as the thermocouples T_1 and T_2 . During the cooling step, there is a difference of $0.22 \pm 0.03 \text{ }^{\circ}\text{C}$ between the controller temperature and the thermocouple measurements. The difference between the recordings of thermocouples T_1 and T_2 during the cooling-heating cycle was

Table 1

Characteristics of emulsions used in cooling-heating cycles, produced by V-FFD.

| Emulsion | A | B | C | D |
|--------------------------------------|------------------|------------------|------------------|----------------|
| Average diameter (μm) | 19.14 ± 0.52 | 25.25 ± 0.97 | 32.75 ± 0.78 | 39.82 ± 2 |
| Water flow rate ($\mu\text{L/hr}$) | 250 | 250 | 250 | 150 |
| Oil flow rate ($\mu\text{L/hr}$) | 25 | 25 | 25 | 75 |
| Valve pressure (Psi) | 22.5 | 16.1 | 0 | 0 |
| Number of droplets | 1801 ± 111 | 1135 ± 51 | 648 ± 8 | 486 ± 20 |
| PDI (%) | 2.9 ± 0.3 | 1.1 ± 0.1 | 3.1 ± 0.1 | 4.8 ± 0.2 |
| Volume fraction (%) | 4.7 ± 0.1 | 8 ± 0.3 | 10.0 ± 0.5 | 13.2 ± 0.6 |
| Surface fraction (%) | 42.0 ± 2.4 | 47.1 ± 0.8 | 45.5 ± 1.6 | 49.6 ± 0.5 |

PDI refers to polydispersity index

0.19 ± 0.02 °C. To determine the temperature variation within the storage channel we measured the temperature at three locations (Fig. S1a) in the serpentine channel (T_1^S , T_2^S , T_3^S), in an empty device (i.e. with no emulsion). Results from these measurements are shown in Fig. S1b, where we see that the average variation between T_1 , T_1^S , and T_3^S is 0.2 °C. However, in the middle of the device, T_2^S shows a variation of 0.6 °C during the coldest stage of the cycle. The larger temperature variation is consistent with the fact that the center of the storage channel is the farthest from the Peltier ring.

2.5. Image processing and data analysis

In both the droplet generation and the temperature cycling experiments, the droplet sizes and counts were measured using a custom-written image processing routine in MATLAB (R2016b, Mathworks). Fig. 2 shows the experimental image and the processed image of the droplets produced using the V-FFD (Fig. 2a) and the droplet array in the storage device (Fig. 2b). From the droplet size and count measurements in the V-FFD, we calculated the mean droplet size and polydispersity index (calculated as the coefficient of variance) of the emulsion for given operating conditions. From the droplet size and count measurements in the storage devices, we calculated the mean droplet size, polydispersity index, and the surface and volume fraction of the emulsions (see Table 1). We also calculated the percentage destabilization of the emulsion due to partial coalescence and the number of coalescence events due to a specified number of individual droplets merging with each other (discussed further below).

To detect the droplets in the images [50], we used the dark interfacial boundary resulting from the mismatch in the refractive index of the water and the oil phase. First, the circular boundary of droplets was identified by converting the images to binary. For more accurate detection of edges, the brightness and contrast of the images were adjusted. Depending on the sharpness of the circular boundary of droplets and the noise in the images, sharpening and softening functions were applied. Then, the images were magnified to ensure the circular liquid droplets were detected in each frame using the circular Hough transform [51]. The detected circles

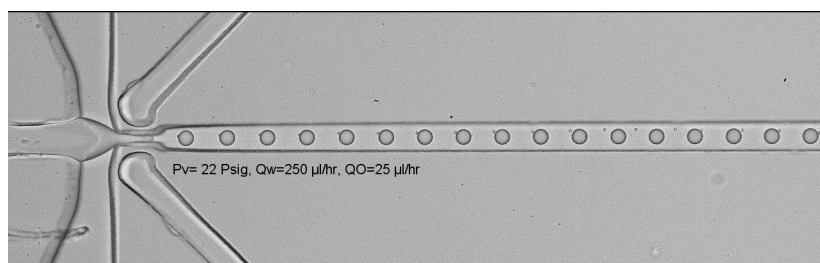
are shown in the bottom panels of Fig. 2a and b colored in blue. We verified the accuracy of the droplet detection algorithm by manually counting the droplets; the error in the number of detected droplets was less than 1%.

In the droplet generation experiments, when the droplet diameter exceeded the channel height, it assumed a pancake shape. Therefore, to convert the measured (or projected) circular diameters D_p to the actual droplet diameter D , we used the following equation [52]:

$$D = \left[h^3 + \frac{3h}{2} (D_p - h) \left(\frac{\pi h}{2} + D_p - h \right) \right]^{\frac{1}{3}} \quad (1)$$

To verify the accuracy in using Equation (1), we have compared the droplet diameters obtained from Equation (1), with the droplet diameters measured outside the droplet generation device where they are spherical. We find the variation in droplet size estimated from these two independent approaches is less than 5%. The mean droplet size, i.e. diameter, and polydispersity index was calculated from a minimum of ≈ 600 droplets. The error bars in the plots indicate the standard deviation from the mean from three experimental replicates. For droplets in the storage device, they all take a spherical shape since the height (≈ 100 μm) of the storage channel exceeds the droplet diameter.

To quantify the extent of emulsion destabilization, we calculate the percentage of coalesced droplets. The number of droplets at the end of the temperature cycle (N_f) can be compared with the number of intact droplets at the beginning of the cycle (N_i) to estimate the percentage of coalesced droplets. However, we do not use this N_i value because we observe that during the heating step, coalescence of the partial crystalline droplets causes adjacent droplets to move out of the field of view (see Supplementary Video 2), thereby not preserving the initial N_i . To quantify the actual number of individual droplets responsible for the destabilized emulsion state at the end of heating step, N_i^* , we use mass conservation. We back-calculate N_i^* as $\sum_{j=1}^{N_f} n_j$, where $n_j = \frac{v_j}{v_0}$. Here, v_j is the volume of the j^{th} droplet in the destabilized emulsion at the end of the heating step and v_0 is the initial droplet volume. Although the number of individual droplets associated with a coalesced drop



Supplementary Video 2.

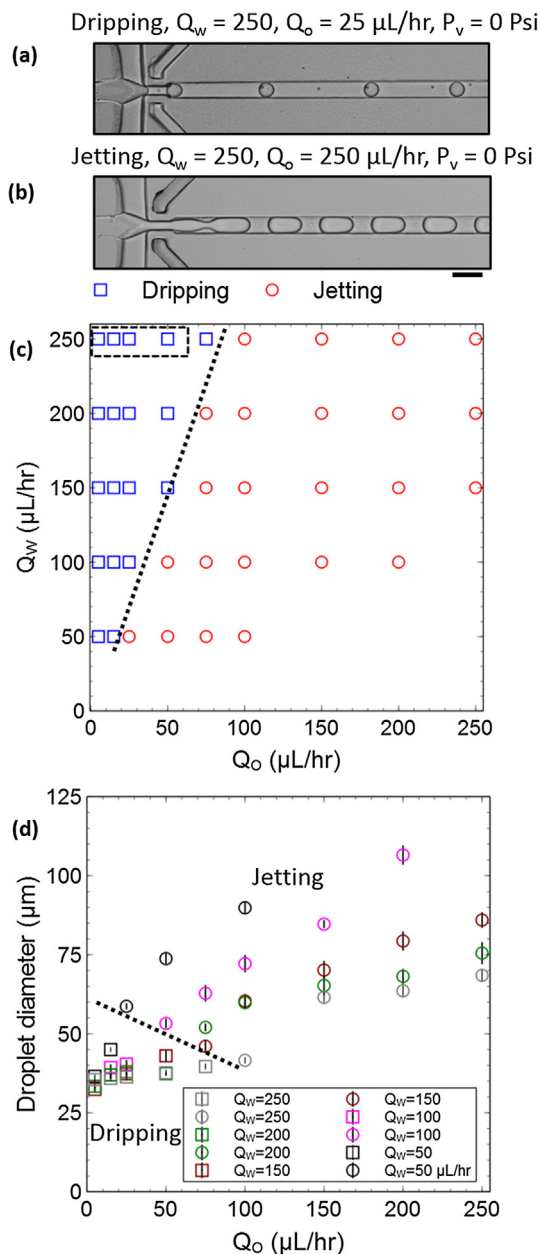


Fig. 3. Droplet generation in V-FFD without valve actuation. Images of droplet generation in V-FFD at (a) dripping and (b) jetting regimes. (c) State diagram denoting flow rate conditions for dripping and jetting regimes. (d) C16 Droplet diameter as a function of oil flow rate for water flow rates of 250 $\mu\text{L/hr}$, 200 $\mu\text{L/hr}$, 150 $\mu\text{L/hr}$, 100 $\mu\text{L/hr}$ and 50 $\mu\text{L/hr}$. At all Q_w values the square and circular symbols are related to dripping and jetting regimes, respectively. The region highlighted with the black bounding box (the top-left) are conditions that were explored with the V-FFD. The dotted lines in (c) and (d) separate the dripping and jetting regions. (For interpretation of the references to color in this figure legend, the reader is referred to the web version of this article.)

is always an integer, we obtain decimal values for n_j which we round-off to their nearest integer values before performing the summation. Thus, we estimate the percentage of coalesced droplets as $(1 - \frac{N_f}{N_t}) \times 100$ and use it as a measure of emulsion destabilization due to partial coalescence.

To understand the destabilization process, we also compute the probability of occurrence of n -body coalescence events, $P(n)$, which denotes what fraction of the droplets at the end of the heating step are due to coalescence between $[n = 2, 3, 4, \dots]$ droplets.

3. Results and discussion

3.1. Droplet generation regimes and size control using the V-FFD

In this study, we employ the V-FFD with the goal of producing HiW emulsions of controlled size for emulsion destabilization studies, particularly with a focus on smaller droplet sizes. We anticipate that the V-FFD, with its ability to vary the orifice width, can provide this flexibility. To identify the relevant operating conditions, we examine the influence of dispersed phase flow rate (Q_o), continuous phase flow rate (Q_w) and valve pressure (P_v). First, we mapped the regimes of dispersed phase behavior without valve actuation and characterized the droplet size distribution. Subsequently, we pursued studies under valve actuation to investigate the flexibility that the V-FFD provides in tuning the droplet size in HiW emulsions (see [Supplementary Video 1](#)).

(a) Without valve actuation

With the valve unactuated, i.e. $P_v = 0$, we observed that the flow focusing device generates droplets in two main flow regimes which have been previously reported in the literature as dripping and jetting [53]. The dripping regime is characterized by the breakup of the dispersed phase at the orifice (see Fig. 3a); whereas in the jetting regime, breakup occurs after the dispersed phase forms a jet, downstream of the orifice (Fig. 3b). We scanned the oil and water flow rates and found that the dripping regime occurs in a narrower flow rate range than the jetting regime (Fig. 3c). We observe that while the dripping regime occurred predominantly at low dispersed phase flow rates, $Q_o < 50$ $\mu\text{L/hr}$, jetting behavior occurred mainly over a wider range of flow conditions, especially for $Q_o > 50$ $\mu\text{L/hr}$, as shown in Fig. 3c.

We quantified the droplet size for all the explored flow conditions. For the water flow rates in the jetting regime, we found that decreasing the oil flow rate significantly reduced the droplet size from 110 to 40 μm as shown in Fig. 3d. With a further decrease in the oil flow rate to $Q_o = 50$ – 100 $\mu\text{L/hr}$, the regime switched to dripping in which the droplet size was much less sensitive to the oil flow rate (Fig. 3c). For instance, in the jetting regime at $Q_w = 100$ $\mu\text{L/hr}$, decreasing Q_o three-fold from 150 to 50 $\mu\text{L/hr}$ decreased the droplet size from 85 to 55 μm . In the dripping regime, however, the same three-fold change from 15 to 5 $\mu\text{L/hr}$ decreased the droplet size from only 40 to 32 μm .

Our characterization of emulsions produced without actuation of the membrane valves shows that smaller droplet sizes could not be obtained in the jetting regime but can be obtained only in the dripping regime. However, the droplet size in the dripping regime could not be varied over a wide range due to insensitivity to flow rate, consistent with observations from prior works [33,54]. Also, without valve actuation, we found the dripping regime was rather narrow. To address these limitations, we used the V-FFD that can potentially expand the range of droplet sizes available in the dripping regime (including droplets with sizes less than 32 μm) by reducing the flow-focusing orifice width via actuation of membrane valves.

(b) Droplet formation in the V-FFD with actuated valve

We investigate the flexibility afforded in accessing smaller droplet sizes by actuating the valve channels and operating in the dripping regime observed in Fig. 3c (The black bounding box highlights these conditions). Specifically, we ran the V-FFD experiments by choosing a higher water flow rate $Q_w = 250$ $\mu\text{L/hr}$ and varying the valve pressure at set oil flow rates of $Q_o = 10, 15, 25$ and 50 $\mu\text{L/hr}$. In Fig. 4a,b, we show that fixing the flow rates but

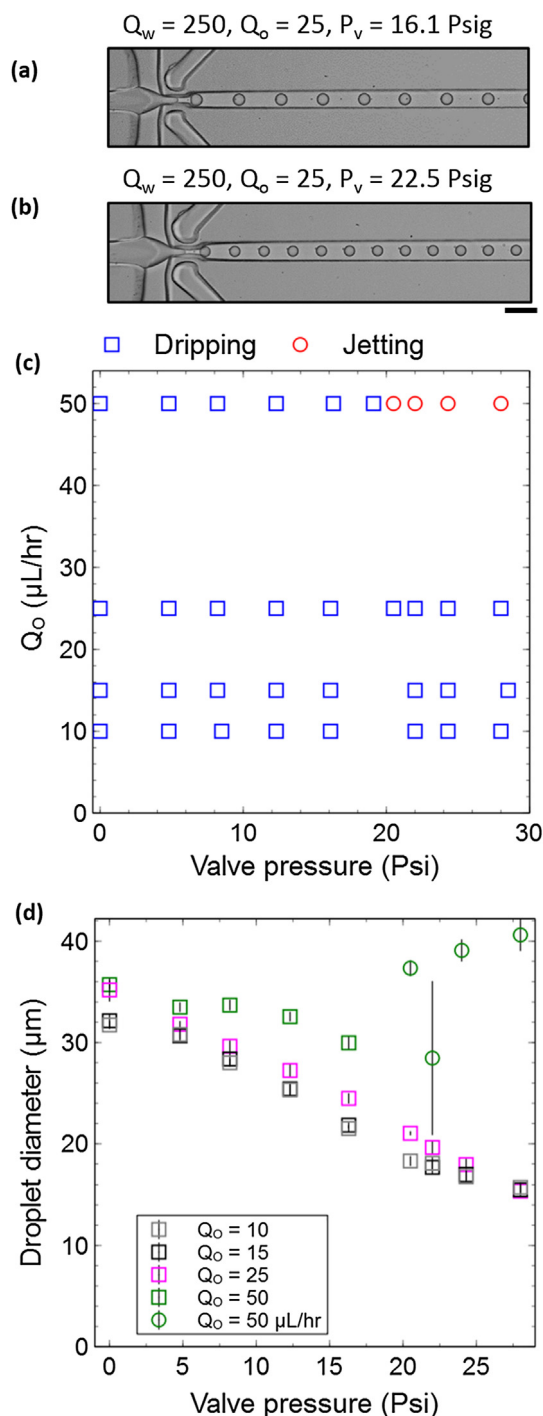


Fig. 4. Droplet generation in the V-FFD with actuated valve. Images of droplet generation in V-FFD at (a) dripping and (b) jetting regimes. The decrease in droplet size when the valve pressure is increased from 16.1 to 22.5 Psig can be visually observed in the images. (c) State diagram showing the flow conditions for dripping and jetting flow regimes. (d) Droplet diameter as a function of valve actuation pressure at $Q_w = 250 \mu\text{L/hr}$ for $Q_o = 10, 15, 25$ and $50 \mu\text{L/hr}$. The square and circular symbols are related to dripping and regimes, respectively. The scale bar is $100 \mu\text{m}$. (For interpretation of the references to color in this figure legend, the reader is referred to the web version of this article.)

changing the valve pressure P_v from 16.1 to 22.5 psi indeed lead to a notable reduction in the droplet size.

In Fig. 4c, we show how varying the valve pressure from $P_v = 0$ – 30 psi influenced the regimes of droplet production for our chosen flow conditions. Overall, we observed a broad regime of

dripping while jetting occurred only for the higher oil flow rate condition of $Q_o = 50 \mu\text{L/hr}$ and for valve pressures greater than ≈ 20 psi. Thus, actuation of the valve widened the dripping regime significantly compared to that without actuation.

Next, we quantified the size of the droplets for the conditions shown in Fig. 4c. We found that except for $Q_o = 50 \mu\text{L/hr}$, the three remaining oil flow rates lead to a linear decrease in the droplet size with an increase in the valve pressure (Fig. 4d). This may be due to the conditions being in the dripping regime where the droplet breakup occurred at the orifice and the valve pressure regulated the orifice width, which controls the droplet size [32]. Interestingly, the droplet size in the jetting conditions (that occurred at high valve pressures >20 psi) is larger even though the size of the orifice is smaller (green circles in Fig. 4d). This is because, in jetting the droplets are produced downstream of the orifice, so their size is not necessarily dictated by the orifice width. In addition, variation in the droplet size in jetting (see error bars in Fig. 4d) are higher than in dripping, indicating that the breakup process is not occurring consistently during jetting. Thus, operating the V-FFD in the dripping regime is optimal for stable generation of monodisperse HiW emulsions.

Now we focus on the actual droplet sizes that can be achieved in the dripping regime. For oil flow rates of $Q_o = 10, 15$ and $25 \mu\text{L/hr}$, we obtained a droplet size range of 36 – $15 \mu\text{m}$ by increasing the valve pressures from 0 to 28 psi. Thus, the V-FFD provides much more flexible control over the size of the droplets, especially when emulsions with smaller droplet size are desired. Based on the results of this investigation, as shown in Table 1, we used $Q_w = 250 \mu\text{L/hr}$ and $Q_o = 25 \mu\text{L/hr}$ at valve pressures of 0, 16.1 and 22.5 psi to generate HiW emulsions with mean droplet size of 32, 25 and $20 \mu\text{m}$. To generate emulsions with droplet size of $40 \mu\text{m}$, we used $Q_w = 150 \mu\text{L/hr}$ and $Q_o = 75 \mu\text{L/hr}$, without valve actuation.

3.2. Mechanisms involved in 2D emulsion destabilization due to partial coalescence

The V-FFD device enables the production of monodisperse HiW emulsions of controlled size. We loaded them into the storage device and investigated the destabilization of the 2D emulsion due to partial coalescence. The images in Fig. 5a show the three main states of the $40 \mu\text{m}$ emulsion at a surface fraction of $\approx 50\%$. At $T = 23^\circ\text{C}$, the droplets are monodisperse and in the liquid phase (Fig. 5a, left). When cooling the emulsion at 1°C/min to 2°C and holding for 20 min, all the droplets become solidified (Fig. 5b, middle). Heating the emulsion leads to partial coalescence, finally turning into a liquid emulsion with polydisperse size distribution (Fig. 5c, right). In this section, we discuss the key mechanisms responsible for emulsion destabilization that we discerned from our experiments using the $40 \mu\text{m}$ emulsion as a representative case.

(a) Destabilization through the formation of small- and large-scale structures

In general, we observe that destabilization in the 2D emulsion proceeds through two steps: (i) During the heating, droplets appear to gradually melt which promotes the formation of small-scale partially coalesced structures. The formation of these structures is evident from the images shown in Fig. 5b, where from $T = 17.0$ to 17.3°C , partially coalesced structures with 2, 3, 4, 5 and 7 droplets are formed. In the images, these structures have been color-coded so that their progression can be easily tracked. Upon further increase in temperature from $T = 17.6$ to 18.1°C , these structures coalesce more and melt completely to form larger spherical droplets. (ii) Because of the high surface coverage of the 2D emulsion, we also observe that large-scale multi-body units

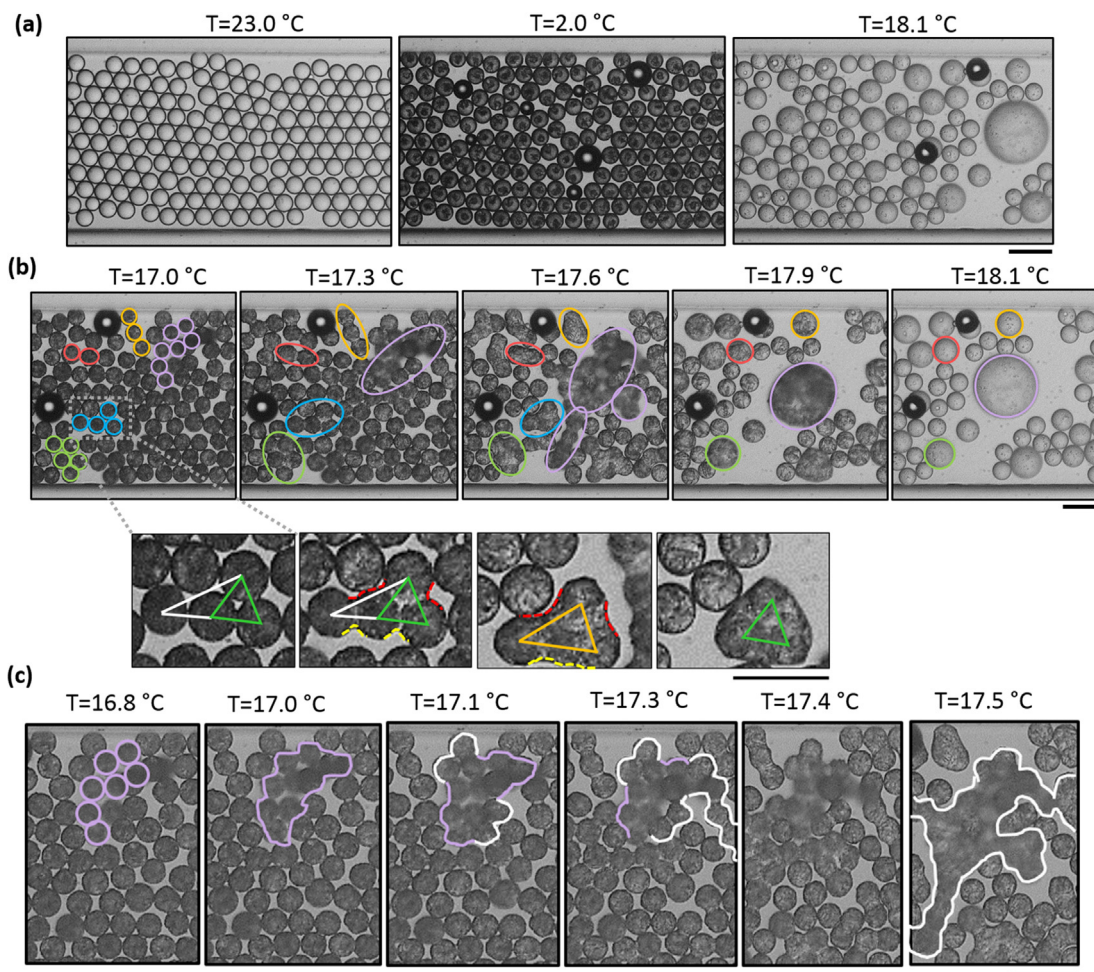


Fig. 5. Process of emulsion destabilization during temperature cycling (a) Images showing droplets of the diameter of 40 μm stored in the storage device at three key steps of the temperature cycling. Light droplets are at liquid phase and dark droplets are crystallized. Changes in the droplet size distribution is visible when comparing the pictures corresponding to the beginning ($T = 23^\circ\text{C}$) and the end of the temperature cycling ($T = 18.1^\circ\text{C}$). (b) Time sequence showing coalescence of partially crystalline of 40 μm C16 droplets. The time step T is 16 s. The evolving merge between 2, 3, 4, 5 and >5 droplets are denoted with red, yellow, blue, green and purple, respectively (See [Supplementary Video 2](#)). The zoomed-inset shows the time sequence of shape transformation of a four-body structure during an 8 s interval. The color-coded angles show the rearrangement of the droplet structure into the compact form of an equilateral triangle driven by the expansion of the two menisci that are highlighted in red. (c) Evolution of the coalescence propagation in 40 μm droplets. Structures highlighted in purple initially start to coalesce. Subsequently, they form new connections with the structures highlighted in white. Scale bars denote 100 μm . (For interpretation of the references to color in this figure legend, the reader is referred to the web version of this article.)

form by coalescence of two or more previously formed smaller structures. This propagation of coalescence in a concentrated emulsion is one of the key steps to promote further destabilization of the emulsion. An example of coalescence propagation is shown in [Fig. 5c](#) where a 7-droplet structure coalesces with four of its adjacent droplets and then merges with additional neighboring structures to form a large-scale aggregate. Interestingly, similar multi-body coalesced structures have been reported in Pickering emulsions in the absence of phase transitions [55].

Thus, our results show that even though small-scale partial coalescence events can spontaneously occur, to induce significant emulsion destabilization (similar to phase inversion) it is necessary to have the propagation of coalescence that leads to large-scale aggregates. We note coalescence propagation has been recently reported by Bremond et al. in a 2D liquid emulsion flowing in a microchannel [56]. They showed that a pair of droplets coalesce while separating due to bulging of interfaces [57]. Invoking this separation-induced coalescence mechanism, they argued that the shape relaxation due to the merging of two liquid drops drives separation of neighboring droplets triggering propagation of coalescence. In our case as well, there is shape relaxation of the

partially coalesced structure during melting, however, we do not observe obvious bulging of interfaces probably because of the semi-crystalline elastic network in the melting droplets. Thus, new mechanisms might be involved in dictating the extent and limits of coalescence propagation.

(b) Restructuring of multi-droplet aggregates during coalescence

An important phenomenon occurring during coalescence is the restructuring of multi-droplet aggregates to a more compact form during the melting step. Dahiya et al. [45] reported a meniscus-driven restructuring mechanism that controls the stability of shapes formed when a third partially crystalline droplet is added to an arrested droplet doublet. They have shown that the expansion of meniscus which connects the droplets will result in the minimization of the surface energy of the triplet via movement of the third droplet to a more compact packing. They have noted that formation of a triangular packing with angles $\sim 60^\circ$ between the droplets is the densest possible arrangements of spheres based on a hexagonal close packing. This densest packing will not be achieved if coalescence arrest is stabilized at larger angles

depending on the solid fraction and initial approach angle of the droplets. Interestingly, similar bond angles of 60° has been reported by Studart et al. [58] during arrested coalescence of particle-stabilized droplets.

Similar to what Dahiya et al. observed, we see the formation of necks that connect the droplets and rearrange them to a more compact form. For example, in the inset of Fig. 5b we follow the restructuring of a quadruplet. Initially, three of these droplets are in the compact form (angle 60°) which is highlighted with green, while highlighted in white are the angles that are not in the compact form ($\sim 30^\circ$). We note that the three bottom droplets are in an almost linear arrangement. It is interesting to see which of the menisci connecting these droplets contribute to restructuring. From the second to the third frame, the bottom two menisci (yellow dashed curves) connecting three droplets of the linear arrangement, although getting more compact due to coalescence, remain in the linear form without any significant movement or change in orientation. In contrast, the two top menisci (red dashed curves) which connect the droplets outside of the linear arrangement move and merge the two top angles, thus primarily contribute to the restructuring. The orange triangle shows an intermediate stage where the expansion of the two top menisci drives the restructuring, and the final green equilateral triangle shows the compact form of this quadruplet.

Thus, the menisci-driven restructuring makes the droplet-aggregates achieve a compact shape during the melting phase. The compaction appears to increase the distance with neighboring droplets thereby reducing the likelihood of small-scale structures to participate in coalescence propagation.

(c) Aggregate growth during coalescence propagation

Although the restructuring mechanism appears to limit coalescence propagation, we do observe instances where large-scale multibody structures form (Fig. 5c and Supplementary Video 2). We suggest that coalescence propagation and growth may involve directional requirements since the large-scale 7-droplet structure shown in Fig. 5c seems to connect with only some of its adjacent droplets preferably. To probe this further, we followed the connections of this propagating multi-droplet structure, as shown in Fig. 6. Since the formation of connections is not very clear in the initial stages of coalescence at this level of magnification and image quality, at each step care is taken to highlight only the connections that obviously have a meniscus, meaning that the corners of the connection line of the two touching droplets are filleted. At $T = 16.5^\circ\text{C}$, 6 of these connections are observed and highlighted in yellow.

In the subsequent step ($T = 16.7^\circ\text{C}$), four more connections are recognized between the initial droplet structure and its surrounding droplets (highlighted in red) indicating coalescence propaga-

tion. The direction of these new connections with respect to the target droplet structure are shown with unidirectional black arrows. Similarly, the new connections formed at $T = 16.9^\circ\text{C}$ are shown along with their unidirectional arrows. In the next step ($T = 17.1^\circ\text{C}$) the number of connections significantly increases due to the formation of connections between the target structure and other multi-droplet structures.

At 17.3°C , the growth of the propagating structure becomes very limited, and the formation of new connections takes place only within the current structure, mainly by the addition of crosslinking connections which form equilateral triangles. These crosslinking connections that are internal to the target structure are shown by bidirectional arrows. Also, we observe that some of the structures do not form cross-linking connections (labeled as blue) and therefore do not participate in the growth process. Thus, the main conclusion we draw from analyzing the aggregate growth process is that the direction of coalescence propagation depends on the availability and orientation of the droplet structures adjacent to a propagating structure. Also, the formation of crosslinking connections which form equilateral triangles is the key to the stability and compaction of large-scale structures and noticeably limits coalescence propagation.

To summarize, destabilization in the 2D emulsion proceeds via formation of both small-scale structures and large-scale droplet structures which form through coalescence propagation. The compaction of the droplet structures due to menisci-driven restructuring reduces the likelihood of coalescence propagation. In contrast, specific geometric orientations of neighboring droplet/structures appear to promote aggregate growth and favor coalescence propagation. Still, the coalescence propagation might be ultimately limited unless internal cross-linking connections are formed.

3.3. Effect of droplet size on destabilization of 2D emulsions

Given that we have identified the key mechanisms in emulsion destabilization, we use the capability of the V-FFD to generate monodisperse emulsions of various droplet sizes and investigate the effect of droplet size on the stability of emulsions to partial coalescence. We chose emulsions with mean droplet sizes of 20, 25, 32 and $40\ \mu\text{m}$, all having a similar surface fraction of $\approx 42\text{--}50\%$. Additional characteristics of these emulsions are listed in Table 1. We performed heating-cooling cycles on the microfluidic emulsions and quantified the degree of emulsion destabilization by evaluating the droplet size distribution in the emulsion at the beginning and end of the cooling-heating cycle. From the droplet size distribution, we also determined how many n -body coalescence events might have occurred that give rise to the final droplet size distribution (see Section 2.5).

In our system, we observe that destabilization occurs through a combination of spontaneous partial coalescence events (that yield

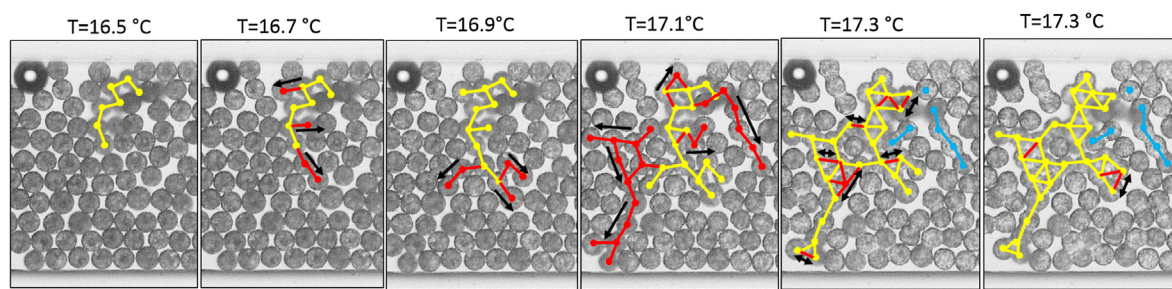


Fig. 6. Growth of an aggregate due to coalescence propagation in $40\ \mu\text{m}$ droplets. A 7-droplet structure highlighted in yellow initially starts to coalesce. Subsequently, it forms new connections with the structures highlighted in red. The blue structures did not participate in propagation. The black unidirectional and bidirectional arrows show the direction of propagation and the crosslink formation respectively. Scale bar denotes $100\ \mu\text{m}$. (For interpretation of the references to color in this figure legend, the reader is referred to the web version of this article.)

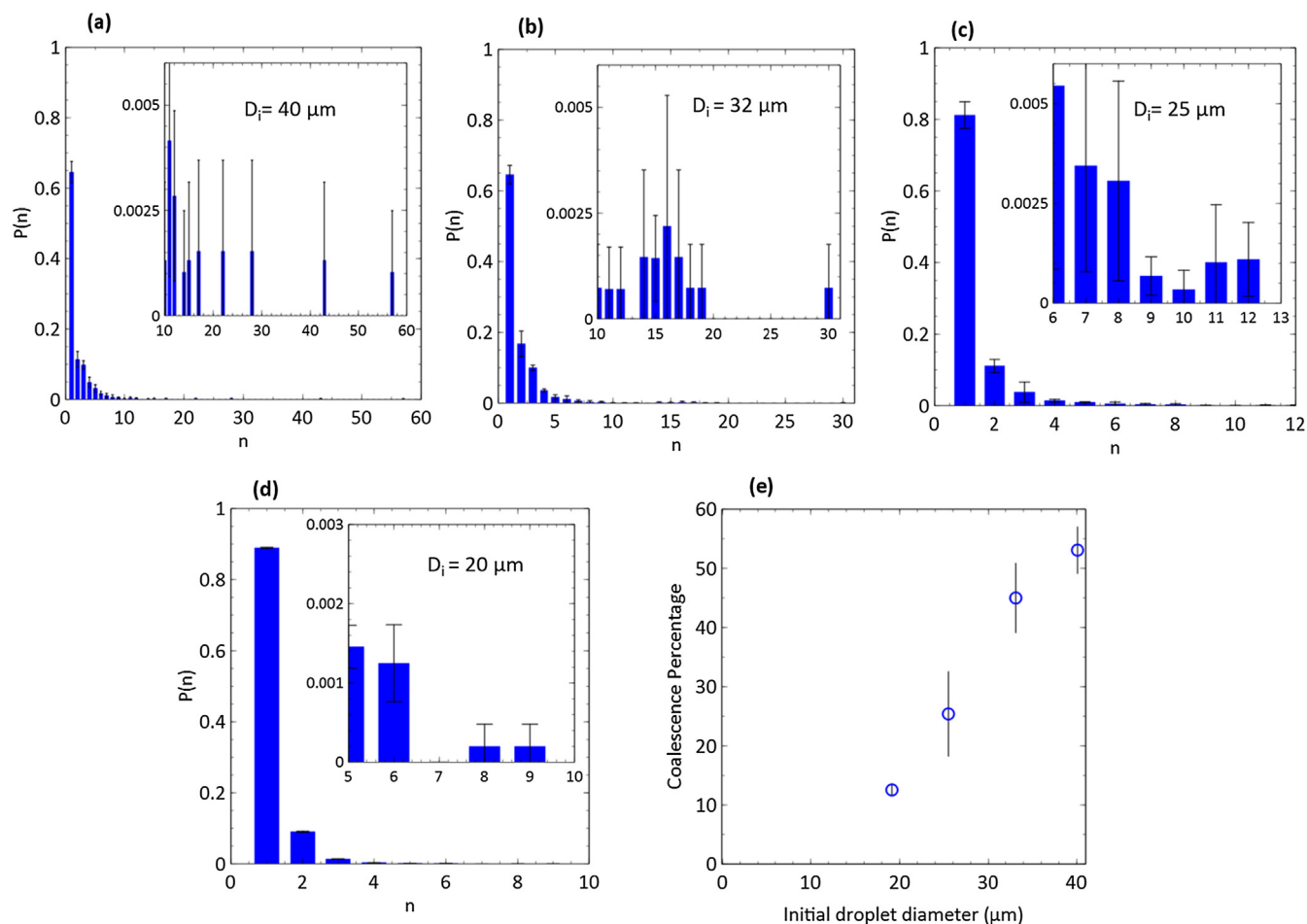
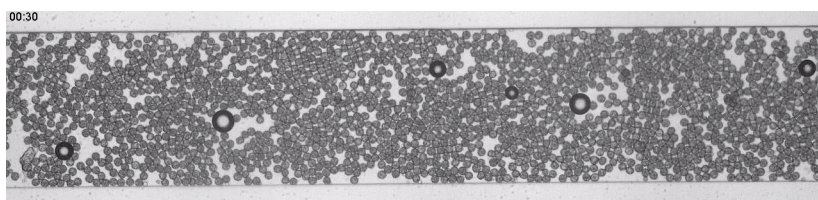


Fig. 7. Effect of droplet size on emulsion destabilization. Probability of n -body coalescence ($n = 1, 2, 3, \dots$) for various droplet diameters (D_i): (a) 40, (b) 32, (c) 25, and (d) 20 μm . In a–d, the insets show a close view of the probability of formation of less frequent larger droplets which mainly form due to coalescence propagation. (e) Plot of coalescence percentage vs. initial mean droplet diameter.

small-scale structures) and coalescence propagation (that yields large-scale structures). Although the formation of multi-droplet structures, both small- and large-scale, is visible from our coalescence movies, it is difficult to track how many structures form over time. Therefore, we did an endpoint analysis by plotting the probability $P(n)$ of n -body coalescence events for the four microfluidic emulsions, as shown in Fig. 7a–d, where we observe two main trends. First, we find that the fraction of intact droplets, $P(1)$, in the final emulsions decreases from around 90% in 20 μm droplets to almost 65% in 40 μm droplets. Second, we observe that the probability of occurrence of larger n -body structures increases with increase in the droplet size. For instance, in the 20 μm -emulsion, we do not observe any structures with >10 droplets (see [Supplementary Video 3](#)), while in the 40 μm -emulsion structures with as high as 58 droplets can form although with rather low probability. Both these observations indicate that emulsions with larger droplets undergo more coalescence, which increases their coalescence percentage - a measure of emulsion destabilization

(Fig. 7e). A two-fold change in droplet size yields about a five-fold increase in emulsion destabilization (Fig. 7e).

The influence of droplet size on emulsion destabilization can be understood by considering how droplet size impacts the initiation of partial coalescence and coalescence propagation. Smaller droplets might be inherently more resistant to initiation of partial coalescence since the combined stress due to disjoining pressure and Laplace pressure needs to be overcome (Filip et al. [59]). In addition to droplet size affecting the probability of initiating partial coalescence, our results show that smaller droplets do not form large-scale multi-body structures. As we discussed before, the formation of these multi-droplet structures requires restructuring into more compact forms during coalescence. With smaller droplets, we expect that the higher curvature of the meniscus connecting them and their inherently less deformability (or higher Laplace pressure) would impose a high energy cost for this restructuring. With regards to coalescence propagation, since smaller droplets have higher energy cost for restructuring, it is less likely that



Supplementary Video 3.

bidirectional internal cross-links form (Fig. S2). Therefore, smaller droplets are less likely to form large-scale multi-body structures, limiting coalescence propagation and the emulsion is less prone to destabilization.

In summary, the droplet size changes the probabilities of initiating partial coalescence, formation of multi-droplet structures, as well as coalescence propagation. This result is significant as previous explanations of emulsion destabilization due to temperature cycling focused largely on single droplet behavior. For example, studies suggest that larger droplets have larger interfacial crystals that protrude more, or they are more 'reactive', thereby increasing the chance of coalescence and its propagation [10,38]. Our study reveals that multi-droplet phenomena including restructuring and cross-link formation need to be incorporated to achieve a complete understanding of emulsion destabilization due to partial coalescence.

3.4. Potential mechanisms initiating partial coalescence

In our study, the focus is on understanding the mechanisms responsible for the 2D emulsion destabilization and how droplet size influences this process. Underlying the destabilization process is the spontaneous coalescence between two quiescent partially crystalline droplets. This initiation of partial coalescence appears to be not well understood. Walstra and co-workers [36] have argued that crystals at the drop interface penetrate a neighboring partially crystalline droplet bridging the two to form a non-spherical structure. Another study suggested that the extent of protrusion of the interfacial crystals determines the ability of the droplets to partially coalesce [38]. More recently, however, it has been shown that coalescence can happen between partially crystalline droplets with no obvious crystal protrusions [40,60]. In our HiW emulsions, we do not observe noticeable crystal protrusions emanating from the drop surface. However, we observe that the droplet surface has a roughness which could be due to crystal partitioning which was previously reported by Ergun et al. [61]. These rough high-curvature regions could locally bring the droplet interfaces close together and trigger partial coalescence.

Another factor that might possibly contribute to the initiation of spontaneous coalescence is the changes in the solubility of surfactant due to crossing the Krafft temperature during the temperature cycling. The Krafft temperature of bulk SDS solutions (critical micelle concentration of SDS: 8 mM [62]) varies from 15.04 to 15.84 °C [63] for surfactant concentration varying from 50 to 85 mM. For the 2 wt% SDS solution (\approx 69.4 mM) we used, the Krafft temperature is estimated to be in the range of 15–16 °C. In our study, we observe that during the cooling step, the droplets are intact (i.e. stable) and the crystallized hexadecane droplets melt during heating at around 17 °C inducing destabilization. Thus, the destabilization temperature is above the Krafft temperature of SDS, suggesting that the partial coalescence-induced destabilization is not affected by the crystallization/solubility of SDS in the continuous phase. However, it is possible that the solubility of surfactant at the droplet interface might change due to the temperature cycling and may contribute to partial coalescence.

4. Conclusions

In this work, we successfully overcame the two main shortcomings of classical studies of partial coalescence [10,36–39,41–44], i.e. polydisperse droplets and indirect measurements, by generating monodisperse and size-tunable hexadecane-in-water microfluidic emulsions, and developing an approach to create 2D arrays of droplets to directly visualize the *in situ* destabilization of these emulsions during thermal cycling. This is significant considering the difficulties associated with partial coalescence studies [36,37]

which rendered the underlying mechanism of how a population of droplets undergo destabilization unexplained.

The use of a V-FFD device in which the orifice width can be flexibly controlled by varying the valve actuation pressure enabled us to generate monodisperse HiW emulsions of droplet size ranging from 40–15 μm in the dripping regime. This expanded range of sizes toward smaller droplets afforded by V-FFD for generation of monodisperse HiW emulsions is significant. As we mentioned earlier, unlike monodisperse water-in-oil emulsions that have been generated at various sizes ranging from 7–200 μm [32], microfluidic monodisperse O/W emulsions have been achieved only over very limited size ranges, for example, 36 and 51 μm in one study [35] and 60–72 μm [17] in another.

Visualizing the destabilization of 2D arrays of these emulsions with a surface fraction of 40–50% showed that destabilization proceeds through a combination of spontaneous coalescence events that yield small-scale structures followed by formation of large-scale structures by coalescence propagation. We observe that before final destabilization, these multi-droplet aggregates restructure to a compact form with 60° bond angles. This re-arrangement was previously reported as the most compact form through which coalescence may proceed in partially crystalline and particle-stabilized droplets [45,58]. Also, we find that coalescence propagation depends on the availability and orientation of droplets and is controlled by the formation of crosslinking connections that unite the segments of the propagating structure via 60° bond angles.

By monitoring emulsion destabilization at four droplet sizes (20–40 μm) we found that the coalescence percentage increases almost linearly with droplet size. Quantifying the probability of *n*-body coalescence events revealed that the fraction of intact droplets is higher for smaller droplet sizes while larger droplets form multi-droplet structures with more members. Therefore, we concluded that the difference in the stability between various droplet sizes arises predominantly from the formation of droplet structures for which coalescence requires restructuring into more compact forms. We expect that higher curvature of the meniscus connecting droplets and higher Laplace pressure of smaller droplets would impose a high energy cost for this restructuring. Therefore, smaller droplet sizes are less likely to form large-scale multi-droplet structures, and consequently, they are more stable. These multi-droplet mechanisms have not been previously reported and extend the classical view of partial coalescence which is based mostly on single-droplet behavior [10,36–39,64,65]. Finally, the simplicity and versatility of our approach open new opportunities to understand not only emulsion destabilization but also a broader range of processes such as nucleation and formation of nonspherical structures.

Acknowledgments

The authors thank the financial support of the Jack Maddox Foundation and National Science Foundation (CAREER: 1150836). We are grateful to Dr. Patrick Spicer and Dr. Swastika Bithi for useful discussions. Scott Hiemstra and Vince Wilde are gratefully acknowledged for assistance with assembly of the pressure control system.

Appendix A. Supplementary material

Supplementary data associated with this article can be found, in the online version, at <https://doi.org/10.1016/j.jcis.2018.08.045>.

References

- [1] J. Bibette, F.L. Calderon, P. Poulin, Emulsions: basic principles, Rep. Prog. Phys. 62 (6) (1999) 969.

- [2] T. Mason et al., Nanoemulsions: formation, structure, and physical properties, *J. Phys.: Condens. Matter* 18 (41) (2006) R635.
- [3] D.J. McClements, Nanoemulsions versus microemulsions: terminology, differences, and similarities, *Soft Matter* 8 (6) (2012) 1719–1729.
- [4] H. Schubert, R. Engel, Product and formulation engineering of emulsions, *Chem. Eng. Res. Des.* 82 (9) (2004) 1137–1143.
- [5] D.J. McClements, Crystals and crystallization in oil-in-water emulsions: implications for emulsion-based delivery systems, *Adv. Coll. Interf. Sci* 174 (2012) 1–30.
- [6] R. Pal, Rheology of simple and multiple emulsions, *Curr. Opin. Coll. Interf. Sci.* 16 (1) (2011) 41–60.
- [7] R. Chanamai, D.J. McClements, Dependence of creaming and rheology of monodisperse oil-in-water emulsions on droplet size and concentration, *Coll. Surf. A* 172 (1) (2000) 79–86.
- [8] K. Boode, Partial Coalescence in Oil-in-Water Emulsions, Agricultural University, Wageningen, 1992.
- [9] P. Taylor, Ostwald ripening in emulsions, *Adv. Coll. Interf. Sci.* 75 (2) (1998) 107–163.
- [10] E. Fredrick, P. Walstra, K. Dewettinck, Factors governing partial coalescence in oil-in-water emulsions, *Adv. Coll. Interf. Sci.* 153 (1) (2010) 30–42.
- [11] H. Feng et al., Manipulating and quantifying temperature-triggered coalescence with microcentrifugation, *Lab Chip* 15 (1) (2015) 188–194.
- [12] S. Hindle, M.J. Povey, K. Smith, Kinetics of crystallization in n-hexadecane and cocoa butter oil-in-water emulsions accounting for droplet collision-mediated nucleation, *J. Coll. Interf. Sci* 232 (2) (2000) 370–380.
- [13] P. Gruner et al., Controlling molecular transport in minimal emulsions, *Nat. Commun.* 7 (2016) 10392.
- [14] R.K. Shah et al., Designer emulsions using microfluidics, *Mater. Today* 11 (4) (2008) 18–27.
- [15] E. Sirota, A. Herhold, Transient phase-induced nucleation, *Science* 283 (5401) (1999) 529–532.
- [16] A.B. Herhold et al., Impurity mediated nucleation in hexadecane-in-water emulsions, *Phys. Rev. E* 59 (6) (1999) 6946.
- [17] T. Krebs, K. Schroen, R. Boom, A microfluidic method to study demulsification kinetics, *Lab Chip* 12 (6) (2012) 1060–1070.
- [18] J. Weiss, N. Herrmann, D. McClements, Ostwald ripening of hydrocarbon emulsion droplets in surfactant solutions, *Langmuir* 15 (20) (1999) 6652–6657.
- [19] B. Spiegel, A. Käfer, M. Kind, Crystallization behavior and nucleation kinetics of organic melt droplets in a microfluidic device, *Cryst. Growth Des.* (2018).
- [20] T.A. Prileszky, E.M. Furst, Fluid networks assembled from endoskeletal droplets, *Chem. Mater.* 28 (11) (2016) 3734–3740.
- [21] N. Denkov et al., Self-shaping of oil droplets via the formation of intermediate rotator phases upon cooling, *Nature* 528 (7582) (2015) 392–395.
- [22] J. Bibette, Depletion interactions and fractionated crystallization for polydisperse emulsion purification, *J. Coll. Interf. Sci.* 147 (2) (1991) 474–478.
- [23] S. Schultz et al., High-pressure homogenization as a process for emulsion formation, *Chem. Eng. Technol.* 27 (4) (2004) 361–368.
- [24] D. Turnbull, R.L. Cormia, Kinetics of Crystal Nucleation in Some Normal Alkane Liquids, *J. Chem. Phys.* 34 (3) (1961) 820.
- [25] L. Mazutis, R. Vasilias, D.A. Weitz, Microfluidic production of alginate hydrogel particles for antibody encapsulation and release, *Macromol. Biosci.* 15 (12) (2015) 1641–1646.
- [26] S.L. Anna, Droplets and bubbles in microfluidic devices, *Annu. Rev. Fluid Mech.* 48 (1) (2016) 285–309.
- [27] E. Brouzes et al., Droplet microfluidic technology for single-cell high-throughput screening, *Proc Natl Acad Sci USA* 106 (34) (2009) 14195–14200.
- [28] J.D. Wehking et al., Effects of viscosity, interfacial tension, and flow geometry on droplet formation in a microfluidic T-junction, *Microfluid. Nanofluid.* 16 (3) (2014) 441–453.
- [29] V. van Steijn, C.R. Kleijn, M.T. Kreutzer, Predictive model for the size of bubbles and droplets created in microfluidic T-junctions, *Lab Chip* 10 (19) (2010) 2513–2518.
- [30] P. Garstecki et al., Formation of droplets and bubbles in a microfluidic T-junction-scaling and mechanism of break-up, *Lab Chip* 6 (3) (2006) 437–446.
- [31] M. Nekouei, S.A. Vanapalli, Volume-of-fluid simulations in microfluidic T-junction devices: Influence of viscosity ratio on droplet size, *Phys. Fluids* 29 (3) (2017) 032007.
- [32] A.R. Abate et al., Valve-based flow focusing for drop formation, *Appl. Phys. Lett.* 94 (2) (2009) 023503.
- [33] Z. Nie et al., Emulsification in a microfluidic flow-focusing device: effect of the viscosities of the liquids, *Microfluid. Nanofluid.* 5 (5) (2008) 585–594.
- [34] P. Umbanhowar, V. Prasad, D. Weitz, Monodisperse emulsion generation via drop break off in a coflowing stream, *Langmuir* 16 (2) (2000) 347–351.
- [35] W.-A.C. Bauer et al., Hydrophilic PDMS microchannels for high-throughput formation of oil-in-water microdroplets and water-in-oil-in-water double emulsions, *Lab Chip* 10 (14) (2010) 1814–1819.
- [36] K. Boode, P. Walstra, Partial coalescence in oil-in-water emulsions 1. Nature of the aggregation, *Coll. Surf. A: Physicochem. Eng. Aspects* 81 (1993) 121–137.
- [37] K. Boode, P. Walstra, A. de Groot-Mostert, Partial coalescence in oil-in-water emulsions 2. Influence of the properties of the fat, *Coll. Surf. A: Physicochem. Eng. Aspects* 81 (1993) 139–151.
- [38] F. Thivilliers et al., Thermally induced gelling of oil-in-water emulsions comprising partially crystallized droplets: the impact of interfacial crystals, *Langmuir* 24 (23) (2008) 13364–13375.
- [39] L. Goibier et al., The effect of surfactant crystallization on partial coalescence in O/W emulsions, *J. Coll. Interf. Sci.* 500 (2017) 304–314.
- [40] A.B. Pawar et al., Arrested coalescence of viscoelastic droplets with internal microstructure, *Faraday Discuss.* 158 (1) (2012) 341–350.
- [41] S.A. Vanapalli, J.N. Coupland, Emulsions under shear—the formation and properties of partially coalesced lipid structures, *Food Hydrocoll.* 15 (4) (2001) 507–512.
- [42] S.A. Vanapalli, J. Palanuwech, J.N. Coupland, Stability of emulsions to dispersed phase crystallization: effect of oil type, dispersed phase volume fraction, and cooling rate, *Coll. Surf. A: Physicochem. Eng. Aspects* 204 (1) (2002) 227–237.
- [43] S. Ghosh, J.N. Coupland, Factors affecting the freeze–thaw stability of emulsions, *Food Hydrocoll.* 22 (1) (2008) 105–111.
- [44] M. Van Boekel, P. Walstra, Stability of oil-in-water emulsions with crystals in the disperse phase, *Coll. Surf.* 3 (2) (1981) 109–118.
- [45] P. Dahiya et al., Arrested coalescence of viscoelastic droplets: triplet shape and restructuring, *Soft Matter* 13 (14) (2017) 2686–2697.
- [46] D.C. Duffy et al., Rapid prototyping of microfluidic systems in poly (dimethylsiloxane), *Anal. Chem.* 70 (23) (1998) 4974–4984.
- [47] P. Wägli, A. Homsy, N.F. de Rooij, Norland optical adhesive (NOA81) microchannels with adjustable wetting behavior and high chemical resistance against a range of mid-infrared-transparent organic solvents, *Sens. Actuators B* 156 (2) (2011) 994–1001.
- [48] S. Koster et al., Drop-based microfluidic devices for encapsulation of single cells, *Lab Chip* 8 (7) (2008) 1110–1115.
- [49] J. Kim, S.A. Vanapalli, Microfluidic production of spherical and nonspherical fat particles by thermal quenching of crystallizable oils, *Langmuir* 29 (39) (2013) 12307–12316.
- [50] A.S. Basu, Droplet morphometry and velocimetry (DMV): a video processing software for time-resolved, label-free tracking of droplet parameters, *Lab Chip* 13 (10) (2013) 1892–1901.
- [51] T.J. Atherton, D.J. Kerbyson, Size invariant circle detection, *Image Vis. Comput.* 17 (11) (1999) 795–803.
- [52] H.-H. Jeong et al., Liter-scale production of uniform gas bubbles via parallelization of flow-focusing generators, *Lab Chip* 17 (15) (2017) 2667–2673.
- [53] G.F. Christopher, S.L. Anna, Microfluidic methods for generating continuous droplet streams, *J. Phys. D Appl. Phys.* 40 (19) (2007) R319.
- [54] A. Abate et al., Impact of inlet channel geometry on microfluidic drop formation, *Phys. Rev. E* 80 (2) (2009) 026310.
- [55] T. Wu et al., Multi-body coalescence in Pickering emulsions, *Nat. Commun.* 6 (2015) 5929.
- [56] N. Bremond, H. Doméjean, J. Bibette, Propagation of drop coalescence in a two-dimensional emulsion: A route towards phase inversion, *Phys. Rev. Lett.* 106 (21) (2011) 214502.
- [57] N. Bremond, A.R. Thiam, J. Bibette, Decompressing emulsion droplets favors coalescence, *Phys. Rev. Lett.* 100 (2) (2008) 024501.
- [58] A.R. Studart, H.C. Shum, D.A. Weitz, Arrested coalescence of particle-coated droplets into nonspherical supracolloidal structures, *J. Phys. Chem. B* 113 (12) (2009) 3914–3919.
- [59] D. Filip et al., Influence of bulk elasticity and interfacial tension on the deformation of gelled water-in-oil emulsion droplets: an AFM study, *Langmuir* 21 (1) (2005) 115–126.
- [60] A. Thiel et al., Coalescence behavior of pure and natural fat droplets characterized via micromanipulation, *J. Am. Oil. Chem. Soc.* 93 (11) (2016) 1467–1477.
- [61] R. Ergun, R.W. Hartel, P.T. Spicer, Kinetic effects on interfacial partitioning of fat crystals, *Food Struct.* 5 (2015) 1–9.
- [62] E. Fuguet et al., Critical micelle concentration of surfactants in aqueous buffered and unbuffered systems, *Anal. Chimica Acta* 548 (1–2) (2005) 95–100.
- [63] C. Vautier-Giongo, B.L. Bales, Estimate of the ionization degree of ionic micelles based on Krafft temperature measurements, *J. Phys. Chem. B* 107 (23) (2003) 5398–5403.
- [64] K. Boode, C. Bisperink, P. Walstra, Destabilization of O/W emulsions containing fat crystals by temperature cycling, *Coll. Surf.* 61 (1991) 55–74.
- [65] J. Giermanska et al., Gelling of oil-in-water emulsions comprising crystallized droplets, *Langmuir* 23 (9) (2007) 4792–4799.